PNAS
www.pnas.org

Supplementary Information for

Structural maturation of cortical perineuronal nets and their perforating synapses revealed by super-resolution imaging

Yaron M. Sigal[1], Haneui Bae[2,3], Luke J. Bogart[2,3], Takao K. Hensch[2,3,4,5]*, Xiaowei Zhuang[1,2,5]*

[1]Howard Hughes Medical Institute, Department of Chemistry and Chemical Biology, Department of Physics, Harvard University, Cambridge, MA 02138, USA
[2]Center for Brain Science, Harvard University, Cambridge, MA 02138, USA
[3]Department of Molecular and Cellular Biology, Harvard University, Cambridge, MA 02138, USA
[4]FM Kirby Neurobiology Center, Department of Neurology, Boston Children's Hospital, Harvard Medical School, Boston, MA 02115, USA
[5]NIMH Silvio O Conte Center, Harvard University, Cambridge, MA 02138, USA
*Corresponding authors: hensch@mcb.harvard.edu (T.K.H.) and zhuang@chemistry.harvard.edu (X.Z.)

This PDF file includes:

SI Materials and Methods

Experimental model and subject details. Animal work was performed in accordance with protocols approved by the Institutional Animal Care and Use Committee at Harvard University and in compliance with all ethical regulations. Wild-type C57B6 male mice of postnatal day 30 (P30) and 90 (P90) were used in our experiments along with P30 MECP2 knockout male mice (RRID:IMSR_JAX:003890) (1). For dark-reared animals, C57B6 mice were raised in the dark from birth and sacrificed at P90. For euthanasia, animals were overdosed (~4ml/kg) with Euthasol (Virbac Animal Health, Fort Worth TX) and perfused with 4% paraformaldehyde in lactated Ringer's solution.

Tissue preparation. Two to three animals were included per condition, and after perfusion fixation with 4% paraformaldehyde, whole brains were postfixed overnight in 4% paraformaldehyde and 60-μm thick coronal vibratome sections were collected through the primary visual cortex (V1). Prior to staining, sections were further trimmed to contain only V1 and the immediate surrounding cortical regions to more easily allow for the processing of multiple sections together.

Immunohistochemistry and embedding. 60-μm thick cortical sections were first blocked for 2-3 hours at room temperature in blocking buffer containing 10% normal donkey serum with 0.2% Triton X-100 and 0.02% sodium azide in 1X Dulbecco's phosphate buffered saline (1X DPBS). Samples were then incubated in primary antibody solutions overnight for 2-3 days at 4^{o}C. Primary antibodies used in this study were rabbit anti-parvalbumin (Swant PV27, 1:200 dilution in blocking buffer), mouse anti-synaptotagmin-2 (Developmental Studies Hybridoma Bank znp-1, 1:200 dilution in blocking buffer), and mouse anti-VGLUT2 (Synaptic Systems 135-411, 1:200 dilution in blocking buffer). Sections were then washed 3 times (each time for 20 minutes) at room temperature in wash buffer (2% normal donkey serum and 0.2% Triton X-100 in 1X DPBS) and incubated in secondary antibody solution overnight at 4^{o}C. The secondary antibodies used were donkey anti-rabbit IgG conjugated to Cy3 (Jackson ImmunoResearch 711-165-152, 1:200 dilution in blocking buffer) and donkey anti-mouse IgG conjugated to Alexa647 (Jackson ImmunoResearch 715-605-150, 1:200 dilution in blocking buffer). Tissue sections were additionally labeled with Wisteria Floribunda Agglutinin (Vector labs, L1350) conjugated to Dy749P1 (Dyomics, 1mg/ml stock, 1:200 dilution in blocking buffer) and Wheat Germ Agglutinin conjugated to Alexa488 (ThermoFisher, W11261, 5mg/ml stock, 1:25 dilution in blocking buffer). Sections were then washed 3 times for 20 minutes each at room temperature in wash buffer followed by 2 times for 20 minutes each at room temperature in 1X DPBS. Samples were post-fixed using 3% paraformaldehyde and 0.2% glutaraldehyde for 2 hours at room temperature and washed 2 times for 20 minutes each at room temperature in 1x DPBS. Prior to dehydration and embedding, areas of V1 were trimmed to remove the meninges and fiber tracts as these structures would undergo a differential shrinkage during processing and this would result in warping of the samples if not removed. Samples to be embedded were dehydrated in a graded series of ethanol (50%, 70%, 95%, and 100%), each step for 15 minutes, and then infiltrated with a graded series of UltraBed epoxy resin/ethanol mixtures (25%/75%, 50%/50%, 75%/25%, 100%/0%, and 100%/0% resin/ethanol, 2 hours each step except that the first 100% resin step was performed overnight). Incubations were done at room temperature on a rotator. Tissue samples in 100% resin were then polymerized by incubation in flat-bottomed BEEM capsules (Electron Microscopy Sciences) at 70^{o}C for 16-18 hours.

Preparation of 70-nm thick tissue arrays for imaging. After embedding, regions of interest containing the highest WFA signal (staining the perineuronal nets) were identified as layer 4 of V1 and samples were

trimmed to be ~300-500 μm in the laminar dimension and centered around layer 4. This resulted in embedded tissue sections that were roughly ~1-2 mm in width across V1, ~300-500 μm in the laminar dimension, and 60 μm thick. From these embedded vibratome sections, ultra-thin sections of 70-nm thickness were cut using an ultra Jumbo diamond knife (DiATOME). Sections were decompressed using chloroform vapor prior to collection on chrom-alum coated coverslips (0.5% gelatin/0.05% chromium potassium sulfate). Coverslips were then dried at 60ºC for 20-30 minutes. Typically, two coverslips each containing ~150 sections were imaged per sample (~300 sections per sample). This number of sections was chosen so that the total thickness of the imaged region was ~21 μm, which is roughly twice the diameter of the soma of PV cells. While samples in embedded blocks showed extraordinary fluorescence stability, once sectioned, samples were imaged within one week. Prior to imaging, samples were chemically etched in 10% sodium ethoxide for 5-20 minutes such that the fluorescent dyes were exposed to the buffer solution to facilitate photoswitching (2), and then washed with ethanol and distilled water and air dried. A mixture of two types of fiducial beads (715/755 0.1 μm carboxylate-modified FluoSpheres and 540/560 0.2 μm carboxylate-modified FluoSpheres, Life Technologies, diluted 1/100 and 1/15 in 1X DPBS, respectively) were spotted (~0.5 μL) onto the coverslip to create a dense field of beads for computationally flattening the illumination field. This mixture was further diluted 1:750 and spotted on the coverslip to create a lower density field of beads for alignment across color channels. Excess beads on the coverslips were immediately washed with distilled water and the coverslips were mounted on glass slide flow chambers. Imaging buffer (10% glucose/17.5μM glucose oxidase/708 nM catalase/10mM MEA/10 mM NaCl/200mM Tris pH 8.0) was added before the chamber was sealed with epoxy.

Microscope setup. The STORM setup was built around a Nikon Ti-E body with a 60x Nikon 1.4NA objective, motorized stage (Prior) and custom pentaband dichroic mirror (zet405-488-561-647-656-752m, Chroma). Lasers (405-nm solid-state laser, Cube 405-100C, Coherent; 488-nm Sapphire HP laser, 500 mW, Coherent; 560-nm fiber laser, 2 W, MPB Communications Inc.; 647-nm fiber laser, 1.5 W, MPB Communications Inc.; 758-nm Toptica tapered amplifier BoosTA system, 1 W, Toptica Photonics) were coupled into the back port of the microscope and used for oblique incidence angle illumination. Fluorescence emission was first reflected off the above custom pentaband dichroic mirror and then passed through an appropriate bandpass emission filter (HQ800/60m for Dy749P1, ET700/75m for Alexa647, ET605/70m for Cy3, and ET525/50m for Alexa488, Chroma) contained in an external motorized filter wheel (Prior) for each probe and detected on the central 600x600 pixel region of a Hamamatsu Orca Flash 4.0v2 sCMOS camera. A 0.7x magnification adapter (Nikon) was also placed before the camera to maintain a 154-nm pixel size. Automated axial focus was maintained using the reflectance off the coverslip of an infrared laser (LP940-SF30, 940 nm, Thorlabs) and detected on a separate CMOS camera (DCC1545M, Thorlabs). Focus was maintained using feedback to a stage nano-positioner (NanoZ, Mad City Labs).

Region of interest (ROI) position identification for automated image acquisition. In our previous version of serial-section STORM (2), the manual selection and position identification of individual regions of interest in each serial section required the largest amount of hands-on microscope time, taking ~1-2 hours for ~50 serial sections. In addition, occasionally errors in manual selection would negatively affect the reconstructed volume. Here, we automated the identification of regions of interest and substantially increased both the accuracy and the speed with which regions of interest could be identified. To accomplish this, the following protocol was applied: Upon mounting the sample, the entire relevant area of the coverslip containing the tissue sections and bead fields (~20 mm x 20 mm) was quickly imaged using a low

magnification 4x objective in order to establish a global coordinate reference system. The PV signal from the soma of the PV+ cells provided readily identifiable features between adjacent sections. From these images, the approximate center of each image was manually identified and a stack of low magnification images was created where each image contained a cropped region of the coverslip centered around a single section. A rigid alignment of the serial sections was done in two steps to identify the translation and rotation (but not scaling) for each section within the global coordinate reference system of the coverslip. The first step was done coarsely based on the image correlation of adjacent sections and the second finer alignment step was based of features of similarity between the adjacent sections. We then switched to the 60x objective and corrected for the small (few microns), variable x-y offset between the objectives by identifying and aligning features in the tissue that were readily identifiable at both magnifications, such as PV+ cell somata. From here, two or three non-overlapping ~100 μm x ~100 μm ROIs were manually selected within the first section of a coverslip. Based on these positions within a single section, the positions for the ROIs within all other serial sections on the coverslip were determined using the transformations calculated from the rigid alignment between sections determined at lower magnification (Fig. S1A). In addition, ~100 μm x ~100 μm fields of view containing an approximately uniform coverage of beads within both high- and low-density bead fields were selected. This procedure was robust across the imaged conditions, required only minimal user input, and could be accomplished in less than one hour for an entire experiment that imaged multiple ROIs over 300 serial sections.

Automated data acquisition. Custom software written in Python was used to control the hardware including the camera, illumination, focus, stage, and emission filter wheel. Prior to beginning data acquisition, a data file interpretable by the software was created that contained all necessary imaging parameters and positions for each ROI to automate the image acquisition. The imaging of each coverslip included the following sequence: First, multiple low-density fluorescent bead fields were imaged across all four color channels. Next, diffraction limited images of each ROI of the sample were acquired across all four color channels. Next, multiple high-density fluorescent bead fields were imaged followed by a second round of imaging of low-density fluorescent bead fields. Finally, STORM imaging was performed for each ROI within the sample. Using the larger-format sCMOS camera (Hamamatsu Orca Flash 4.0v2), we imaged each ROI with a single ~100 μm x ~100 μm field of view. Switching of color channels were achieved by sequentially selecting separate emission bandpass filters for each fluorescent probe in an automated manner using a motorized emission filter wheel. Due to the heterogeneity within the cortex, the two infrared laser reflection spots (for autofocusing) were sometimes differentially scattered leading to an inaccurate estimation of the focal position of the sample (by up to hundreds of nanometers). Instead of assuming a fixed focal position at each section, upon moving to a new position, a rapid axial sweep in 100-nm increments from 1 μm below to 1 μm above the predicted focal plane was performed while imaging at low intensity (5 mW) in the 488-nm channel. The optimal focal plane was then determined for each position by approximating the total image contrast for each image at each axial position, and determining the axial position which maximized the image contrast. To ensure that all images were collected at an optimal focal plane, we also corrected for the axial chromatic aberration of our optical path in the four color channels. To correct for this, after determining the focal position based on the 488nm channel, additional offsets of 300 nm, 200 nm, and 100 nm were applied when acquiring data in the 750-nm, 647-nm, and 561-nm channels, respectively. Data was initially written to local solid state drives and after completion of the acquisition of each STORM movie, the data was immediately transferred to storage at the FAS Division of Science, Research Computing Group at Harvard University for image reconstruction.

Volumetric image reconstruction. The single molecule fitting, image processing, and three-dimensional reconstruction of volumetric superresolution datasets was performed on the Odyssey cluster at the FAS Division of Science, Research Computing Group at Harvard University. Each frame of a STORM movie was analyzed using DAOSTORM (3, 4) to determine the localizations of each individual molecule. The lateral chromatic aberration was corrected for both rendered STORM images and diffraction limited images using third order polynomial transform maps between the four color channels. These transformations were generated using thousands of isolated fluorescent beads (low-density fields of beads) mapped over the entire imaging field and the residual error after chromatic aberration correction was <10nm across the field of view. STORM images of each physical section were analyzed in parallel using single CPU cores with a memory allocation of ~4GB. Once all individual physical sections were analyzed, serial-section alignment of the entire dataset was run as a single process using multiple cores (32 cores) and ~30GB of RAM. Serial-section alignment was performed in two stages, first as a rigid alignment which provided a coarse alignment of the dataset, followed by an elastic registration based on the entire dataset to correct for local distortions between sections that arose during the ultra-thin sectioning of the tissue (2, 5). The resulting STORM image was then filtered to remove spurious intensity that arose due to occasional debris on the coverslip. This was performed by applying a mask based on the corresponding thresholded, diffraction limited images, where the diffraction limited images were thresholded using the lower value of a two-level Otsu threshold. Additionally, to correct for small variations in section thickness and any changes in imaging conditions throughout an experiment, the intensity of the images was smoothed across adjacent sections. This was performed by normalizing the intensity image histogram for each section to a rolling average histogram determined from several adjacent sections. Three-dimensional surface rendering was also performed on the Odyssey cluster using the 3D Viewer plugin in Fiji using large memory allocations or a virtual frame buffer in one or two-colors. In these surface renderings, the surface intensity value was generally set based on the higher value of a two-level Otsu threshold, and 360° rotations of the surface renderings were saved as movies.

WFA-positive cell selection. In each ~100 μm x ~100 μm x ~20 μm image volume, multiple PV+ soma with positive WFA signal (staining the perineuronal nets) were manually identified and a bounding box surrounding the soma and proximal neurites of each cell was cropped for further analysis. Cells that were near the edge of the image acquisition volume were sometimes not imaged well and discarded. In addition, only cells containing more than 5 μm of imaged depth were retained. As some partially imaged cells were then included for further analysis, each cell data point was weighted by an approximation of the fraction of the cell that was imaged.

In addition to WFA+ PV+ soma, a small fraction of WFA+ somata were identified as PV-negative (PV-) across all conditions (wild-type (WT) P90 cells, WT P30 cells, dark-reared (DR) P90 cells, and $MeCP2^{-/y}$ P30 cells), with WFA+ PV- cells appearing more abundantly in tissue from DR P90 animals than in other conditions. For PV+ cells, a small fraction of somata were identified as WFA-negative (WFA-) across all four conditions described above, with a greater percentage of WFA- PV+ cells observed in WT P30 animals than in WT P90 animals. Due to the limited number of imaged examples for both WFA+ PV- and WFA- PV+ cells within layer 4 of the cortex, we did not perform further quantitative comparison of these populations.

Surface projection of the PNN image. To begin, high intensity WFA signal within each imaged section was selected using the Otsu method, and the soma of each PV+ cell was fit to a sphere. The WFA signal

was centered to this sphere, and transformed from Cartesian coordinates (x,y,z) to spherical coordinates (r, θ, φ) using inverse transformations. Next, an equal-area world-map-like projection was created by applying a cylindrical transformation to the spherical coordinates (θ, φ) to obtain (θ', z') while maintaining the spherical coordinate r as a third dimension Z' that is orthogonal to (θ', z') in the cylindrical projection coordinates. To create an equal-areal cylindrical projection across the surface of each cell, the Behrmann projection was used which models a cylinder that intersects the fit sphere of the cell at 30° above and below the identified center (θ = 60° and 120°) creating no linear distortion at these two parallels. Within this projection, positive stretching of apparent distances in the θ' dimension closer to the poles (at larger z') and negative stretching of apparent distances in the θ' dimension closer to the center (at smaller z') is compensated by non-linear spacing of θ in z' which compresses objects in z' closer to the poles. While this class of projections introduces some distortion of shapes and distances away from the two intersecting parallels, it accurately maintains the relative areas of objects at the same Z' across the entire projection thereby allowing the measurement and comparison of object areas within these datasets. In addition, to remove extreme distortion at large z', Behrmann projections were cropped at 85° above and below the identified center. Next, to transform the WFA signal to a planar reference surface that more accurately represents the non-spherical and irregular surface of the cell, the third orthogonal dimension (Z') of the Behrmann projection was modified by fitting the WFA signal in the Behrmann projection to a two-dimensional spline and subtracting the calculated Z' values of this fit from the Z' values of the WFA signal. For each dataset, this set of transformations was first determined using the WFA signal and subsequently applied to the synaptic channel.

Quantification and statistical analysis. Quantification and statistical analysis was performed in Matlab using existing statistical functions including the two-sided Kolmogorov-Smirnov test. Details of the quantification can be found both in the Results section of the text as well as in the figure legends with additional notes provided in this section. No data was excluded from analysis and the non-parametric Kolmogorov-Smirnov test was used to avoid assumptions regarding the underlying distribution of the data.

To facilitate the comparison of WFA and synaptic signals across WFA+ cells, we performed analysis of the WFA and synaptic signals on two different surface intensity projections in the radial dimension based on maximum intensity projections of 70-nm and 500-nm thickness centered around the position of highest WFA intensity on the cell surface. We performed the principal component analysis based on several morphological or statistical parameters of the PNN (WFA) signal, including the mean hole size, the contiguity, the WFA surface intensity, the mean WFA+ intensity, the WFA surface fraction, the WFA signal contrast, the skew of the WFA signal, and the uniformity of the WFA signal, as defined below. The mean hole size is defined as the mean effective radius of the holes within the PNN after WFA signal thresholding, where the effective radius of a hole is determined as the radius of a circle with the same area as the hole, and thresholding was performed with a local Otsu threshold with a window of 1 μm. The contiguity is defined as the fraction of WFA signal that resides within the largest connected component of the WFA signal after signal thresholding. The WFA surface intensity is defined as the mean WFA intensity across the entire projection surface. The mean WFA+ intensity is defined as the mean WFA intensity within the WFA positive region, after thresholding as described above. The WFA surface fraction is defined as the fraction of cell surface area that is WFA+ after thresholding. The WFA signal contrast is defined by the standard deviation of the probability distribution function of the WFA intensity, $\sqrt{(\sum(z_i-m)^2*p(z_i))}$, where $p(z_i)$ is the probability distribution function of the WFA intensity, and m is the mean intensity. The

skew of WFA signal is defined as the third central moment of the probability distribution function of the WFA intensity normalized by the intensity range, i.e. $(\sum(z_i-m)^3*p(z_i))/(L-1)^2$, where L is the range of possible intensities. A Gaussian distribution would give a value of 0 for the skew metric, while those with a long right tail will give positive values and those with a long left tail give negative values. The uniformity of the WFA signal is defined as $\sum(p^2(z_i))$.

Analysis was performed on the entire surface of the imaged WFA+ cell soma, but when displaying the equal-area cylindrical Behrmann projection, we typically only presented the center portion (~5 μm x ~15 μm), or smaller subsets of the projection images to highlight the details of the net and synaptic contacts.

To test if cell shape changes with PV cell maturation, we quantified three parameters measuring the size, sphericity, or ellipticity of the cell soma (Fig. S2): 1) the effective radius of the PNN as determined by fit of the PNN signal to a sphere (Fig. S2A), 2) the goodness of fit of the PNN to a sphere (R^2, defined as 1 - (sum of squares of the spherical fit residual)/(sum of squares of the total WFA variance) (Fig. S2B), 3) the ellipticity of the best fit ellipsoid maintaining two equal semi-axes. Specifically, the ellipticity is calculated for the best ellipsoidal fit and defined as $\sqrt{((C^2 - A^2)/C^2)}$ where C is the longest semi-axis and A is the shortest semi-axis (Fig. S2C). Only the most complete imaged cells (>400 μm^2 of imaged surface area) were included in these analyses in order to provide a more accurate measurement. These cell-shape parameters did not change substantially across the four conditions of animals studied in this work (WT P90, WT P30, DR P90, $MeCP2^{-/y}$ P30) and showed little statistically significant correlation with the WFA surface intensity as determined by a two-sided Kolmogorov-Smirnov test (Fig. S2).

To analyze the Syt2 signal in three-dimensions in Cartesian coordinates, the signal was filtered with a Gaussian function with $\sigma = 60$ nm, thresholded using the global Otsu method, and connected components of synaptic signal were identified in three-dimensions.

Data and software availability. The data that support the findings of this study are available upon request. Custom analysis scripts were written in a combination of Python, Matlab, and Jython and executed on the Odyssey computing cluster. Analysis software used in this study are available upon request.

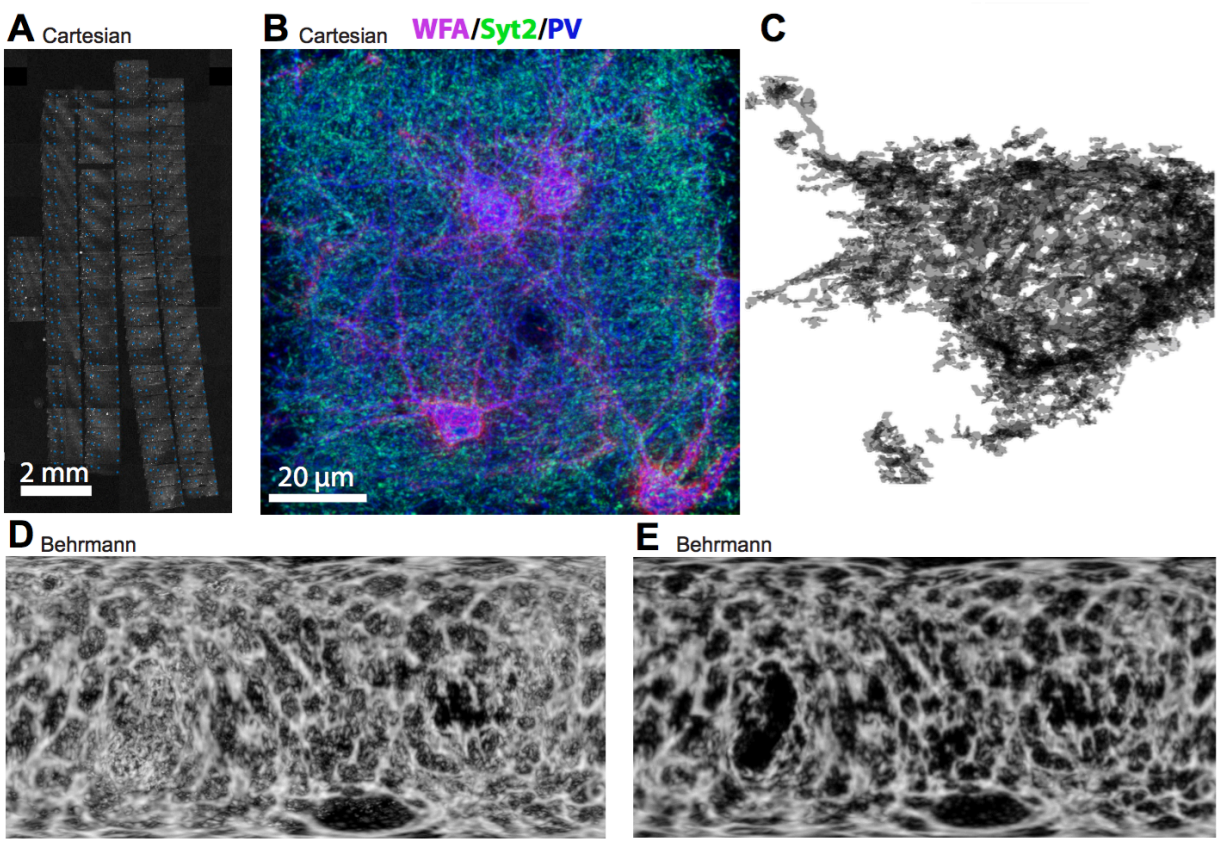

Figure S1. Three-dimensional reconstruction of PV+ cells with surrounding PNNs via serial-section STORM imaging and visualization of the PNN signal surrounding a PV cell using the Behrmann equal-area cylindrical surface projection. **(A)** Overview of a coverslip showing serial sections imaged in the PV channel and overlaid with the positions of three regions of interest (ROIs) (blue dots) that were imaged during data acquisition. Scale bar: 2 mm. **(B)** A composite maximum intensity projection STORM image in Cartesian coordinates of the three channels, WFA (labeling the PNN, magenta), Syt2 (green), and PV (blue), presented for a typical ~100 µm x ~100 µm field of view and 20 µm total thickness centered around layer 4 of the primary visual cortex. **(C)** The WFA signal surrounding a PV+ cell. **(D)** The WFA signal shown in (C) is transformed from Cartesian coordinates (x, y, z) first to spherical coordinates (r, θ, φ). The spherical coordinates (θ, φ) was then mapped on to cylindrical coordinates (θ', z') using an equal-area cylindrical surface projection (Behrmann projection, SI Materials and Methods), while the spherical coordinate r is maintained as a third dimension Z' that is orthogonal to (θ', z') in the Behrmann projection coordinates. Shown here is the maximum intensity projection in the Z' dimension through the entire surface after the above described transformation. **(E)** The WFA signal shown in (D) is next transformed into a reference frame that more accurately represents the non-spherical and irregular surface of the cell. This is done by fitting the WFA signal to a two-dimensional spline and subtracting the offset from the Z' position of the WFA signal. The maximum intensity projection through a 500-nm thickness along the Z' direction centered around the peak of the WFA signal is shown.

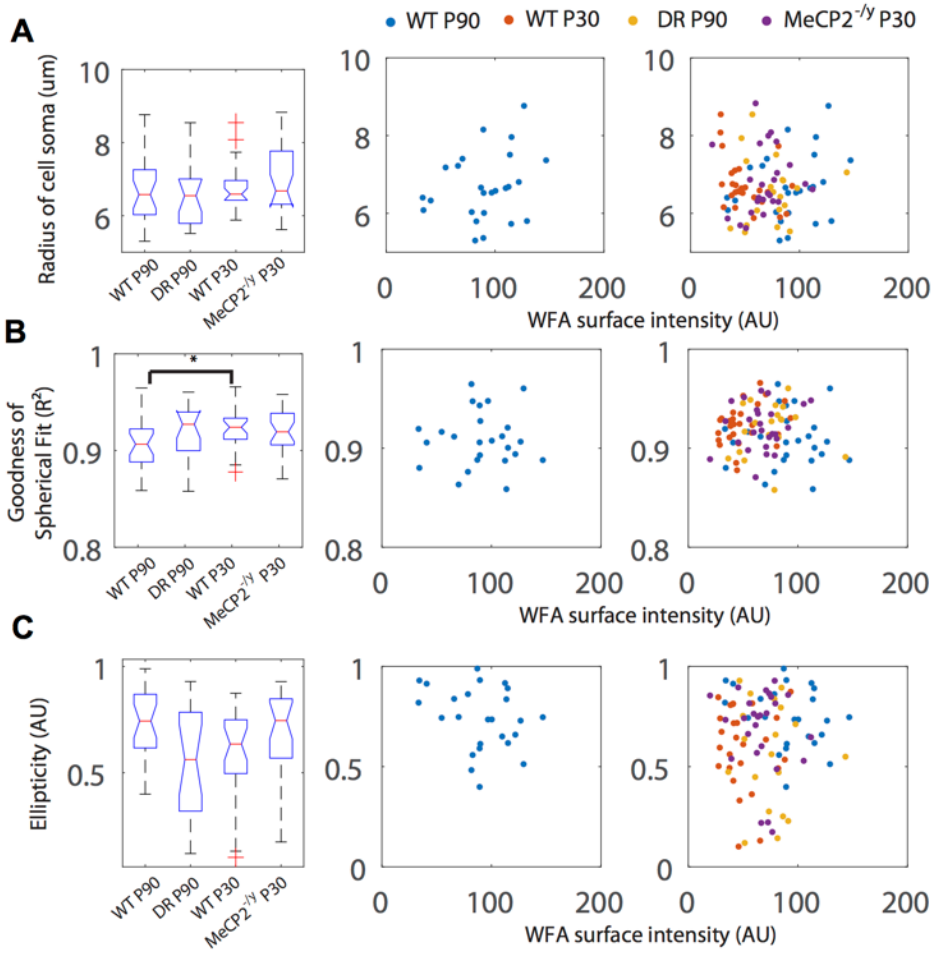

Figure S2. **PV cell size and shape variation as a function of condition and WFA intensity. (A)** Left panel: Box and whiskers plot for the effective radius of the PNN enwrapping PV+ cell soma across the four conditions (wild-type (WT) P90 cells, WT P30 cells, dark-reared (DR) P90 cells, and MeCP2$^{-/y}$ P30 cells). Radii are determined based on the fit of the WFA signal of each cell to a sphere. As radii are calculated based on WFA signal within the extracellular space, including signal surrounding proximal neurites, these measurements likely represent a slight overestimation of the true radii of these cells. Red line denotes median values; notches denote a 95% confidence interval around the median; boxes denote the 1st and 3rd quartiles of the data; whiskers denote the expected 99% values assuming a normal distribution; outliers are shown as red crosses. Center panel: Bivariate plot of the effective radius value versus the WFA surface intensity. Each dot represents a single cell at P90. Right panel: Same as the center except each color-coded point represents a cell within a given condition. Blue: WT P90, Red: WT P30, Yellow: DR P90, and Purple: MeCP2$^{-/y}$ P30. **(B)** Same as (A) but for the goodness of fit (R^2) of the WFA signal to a sphere as a metric instead of the effective radius of the PNN. R^2 is defined as: 1 - (sum of squares of the spherical fit residual)/(sum of squares of the total WFA variance). **(C)** Same as (A) but for the ellipticity as a metric instead of the effective radius of the PNN. Ellipticity is calculated from the best ellipsoidal fit of the PNN signal that maintains two equal semi-axes and is defined as $\sqrt{((C^2 - A^2)/C^2)}$ where C is the longest semi-axis and A is the shortest semi-axis. Statistical significance is determined by a two-sided Kolmogorov-Smirnov test. * P<0.05 and only significant tests are labeled on the box plots.

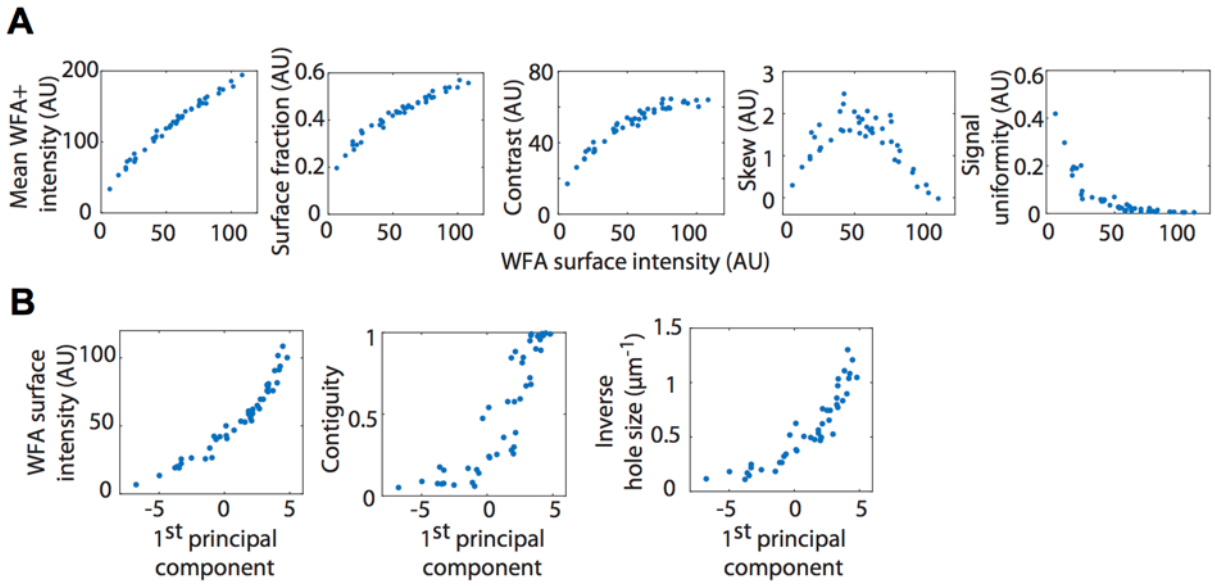

Figure S3. Additional characterization of the PNN structural metrics. (A) Bivariate plots of WFA surface intensity versus various other structural metrics of the PNNs used for principal component analysis. Each dot represents a single cell at P90. Mean WFA+ intensity is defined as the mean intensity within WFA+ regions. Surface fraction is defined as the fraction of surface area that is WFA+. Contrast is defined by the standard deviation of the probability distribution function of the WFA intensity. Skew is defined as the third central moment of the probability distribution function of the WFA intensity normalized by the intensity range, i.e. $(\sum(z_i\text{-}m)^3*p(z_i))/(L\text{-}1)^2$. A Gaussian distribution would give a value of 0 for the skew metric, while those with a long tail on the right will give positive values and those with a long tail on the left will give negative values. Uniformity is defined as $\sum(p^2(z_i))$. For the above metrics, $p(z_i)$ is the probability distribution function of the WFA intensity, m is the mean intensity, and L is the range of possible intensities. **(B)** Bivariate plots of the first principal component in the principal component analysis as shown in Fig. 1E versus WFA surface intensity, contiguity, and hole size (plotted as 1/hole size), as defined in Fig. 1D.

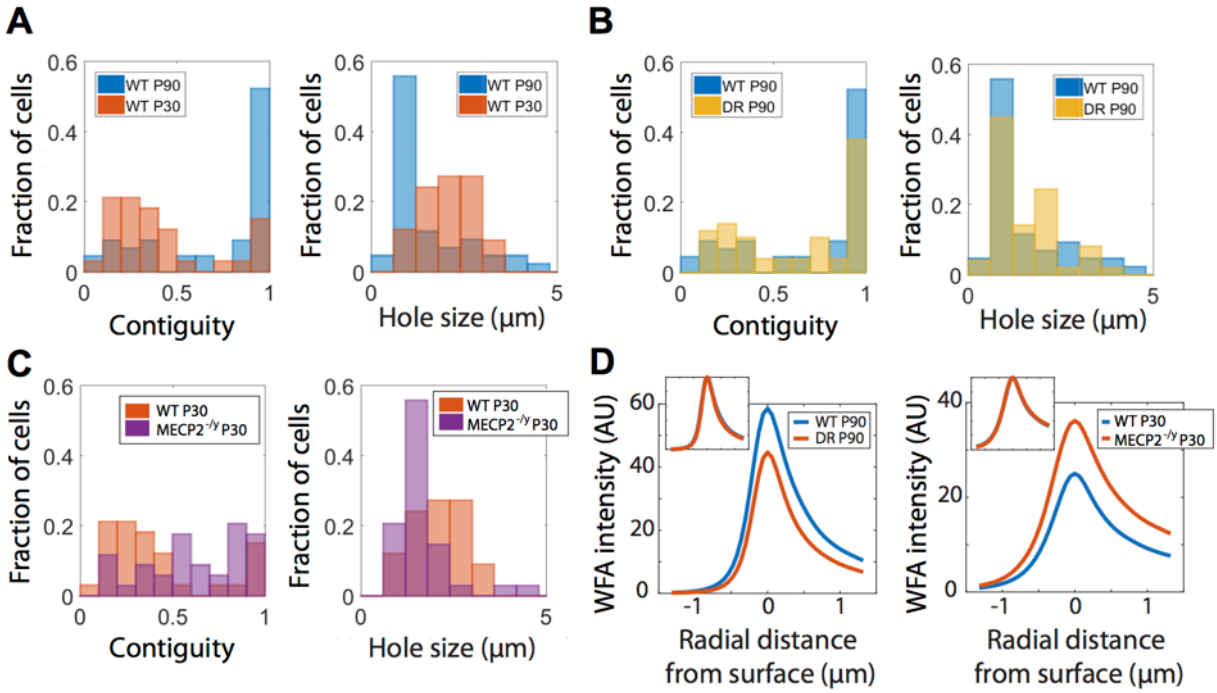

Figure S4. Additional quantification of PNN morphology during development and in dark-reared (DR) animals and MeCP2-deficient animals. (**A-C**) Probability distribution functions of the contiguity of the PNN signal and the mean hole radius of the PNNs surrounding WFA+ PV+ cells under various conditions. Contiguity and mean hole size are defined as in Fig. 1D. **(A)** For cells from wild-type (WT) P90 (blue) and P30 (red) animals (the contiguity distribution is also shown in Fig. 2B). **(B)** For cells from WT (blue) and DR (yellow) P90 animals. **(C)** For cells from WT (red) and MeCP2$^{-/y}$ (purple) P30 animals. **(D)** Left: Average radial intensity distributions of WFA signal surrounding WFA+ PV+ cells in DR animals (red) at P90 in comparison with the age-matched control animals (blue). Insets show the radial distributions normalized to the peak WFA intensity. Right: Same as left but for the comparison between MeCP2$^{-/y}$ (red) and age-matched control animals (blue) at P30.

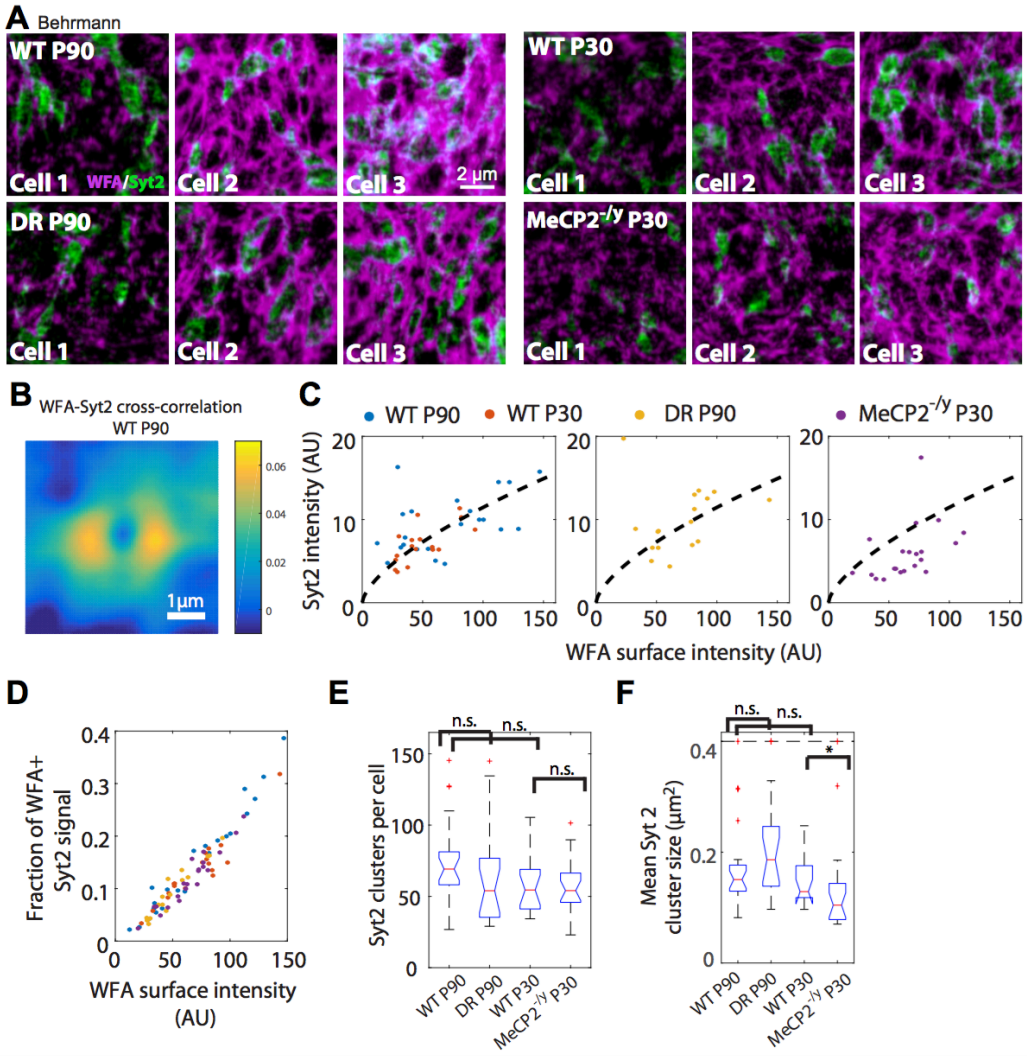

Figure S5. Additional quantifications of Syt2 signals across conditions. (A) Behrmann equal-area cylindrical surface projection of two-color STORM images of WFA (magenta) and Syt2 (green) of regions of WFA+ PV+ cells. Cells representing a range of PNN intensities are shown for wild-type (WT) P90, WT P30, dark-reared (DR) P90, and MeCP2$^{-/y}$ P30 conditions. Only a representative portion of each cell is shown in each image. The WT P90 images are reproduced from Fig. 4A. Scale bar: 2 µm. A scale bar is included for these small-area Behrmann projections as the non-linear distortion is small over such small areas. **(B)** Two-dimensional normalized cross-correlation of Syt2 signal with the WFA signal over the cell surface from WT P90 animals. The cross-correlation was computed for each cell in the Behrmann projection and then averaged over all cells. Scale bar: 1 µm. **(C)** Plot of Syt2 surface intensity (I_{Syt2}) versus WFA surface intensity (I_{WFA}). Each color-coded point represents a cell within a given condition. Left: For cells from WT animals at P90 and P30. Center: For cells from DR P90 animals. Right: For cells from MeCP2$^{-/y}$ P30 animals. Dashed lines: power-law function fit ($I_{Syt2} = \beta * I_{WFA}^{\alpha}$) of WT P90 and P30 cells. The scaling exponent $\alpha = 0.65$. **(D)** Bivariate plot of the fraction of Syt2 signal that overlaps with the WFA signal versus the WFA surface intensity. Each color-coded point represents a cell within a given condition. Blue: WT P90, Red: WT P30, Yellow: DR P90, and Purple: MeCP2$^{-/y}$ P30. **(E)** Box and whiskers plot for the number of Syt2 clusters per cell across the four conditions. **(F)** Box and whiskers plot for the mean physical size (area) of Syt2 clusters per cell across the four conditions. Elements in the box and whiskers plot are as defined in Fig. 4. Statistical significance is determined by a two-sided Kolmogorov-Smirnov test. n.s. $P>0.05$, * $P<0.05$, ** $P<0.01$, *** $P<0.001$.

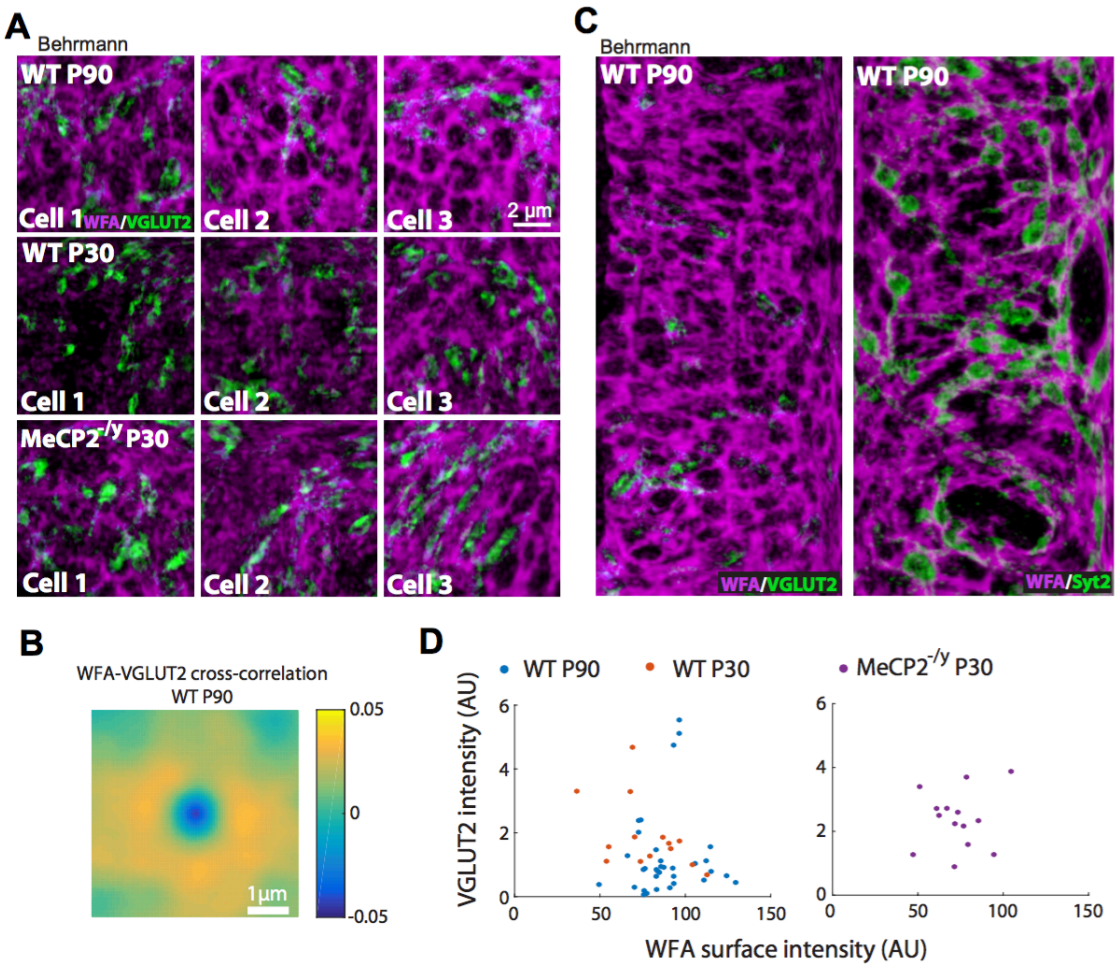

Figure S6. Additional quantifications of VGLUT2 signals across conditions. (A) Behrmann equal-area cylindrical surface projection of two-color STORM images of WFA (magenta) and VGLUT2 (green) of regions of WFA+ PV+ cells. Cells representing a range of PNN intensities are shown for wild-type (WT) P90, WT P30, and MeCP2$^{-/y}$ P30 conditions. Only a representative portion of each cell is shown in each image. Scale bar: 2 µm. A scale bar is included for these small-area Behrmann projections as the non-linear distortion is small over such small areas. **(B)** Two-dimensional normalized cross-correlation of VGLUT2 signal with the WFA signal averaged over all cells from WT P90 animals. The cross-correlation is as calculated in Fig. S5B. Scale bar: 1 µm. **(C)** Behrmann equal-area cylindrical surface projection of a PNN enwrapping a PV+ cell and VGLUT2+ excitatory and Syt2+ inhibitory synaptic contacts perforating the PNN. Equal-area cylindrical surface projections of WFA (magenta) and synaptic (green) signals of a 500-nm thick region centered around the radial peak of the WFA signal are shown. Left: VGLUT2, Right: Syt2 (reproduced from Fig. 1B). **(D)** Plot of VGLUT2 surface intensity (I_{VGLUT2}) versus WFA surface intensity (I_{WFA}). Each color-coded point represents a cell within a given condition. Left: For cells from WT animals at P90 and P30. Right: For cells from MeCP2$^{-/y}$ P30 animals. The distribution of VGLUT2 values was shifted towards higher values for WT P30 cells as compared to WT P90 cells. However, we observed a few outlier WT P90 cells that showed higher values of VGLUT2 surface intensity than the highest VGLUT2 values observed for the P30 cells. The synaptic clusters on these outlier cells appeared qualitatively similar to those observed on the other cells, only with higher cluster abundance. Due to the small number of such cells, it is unclear whether these cells represent a distinct population.

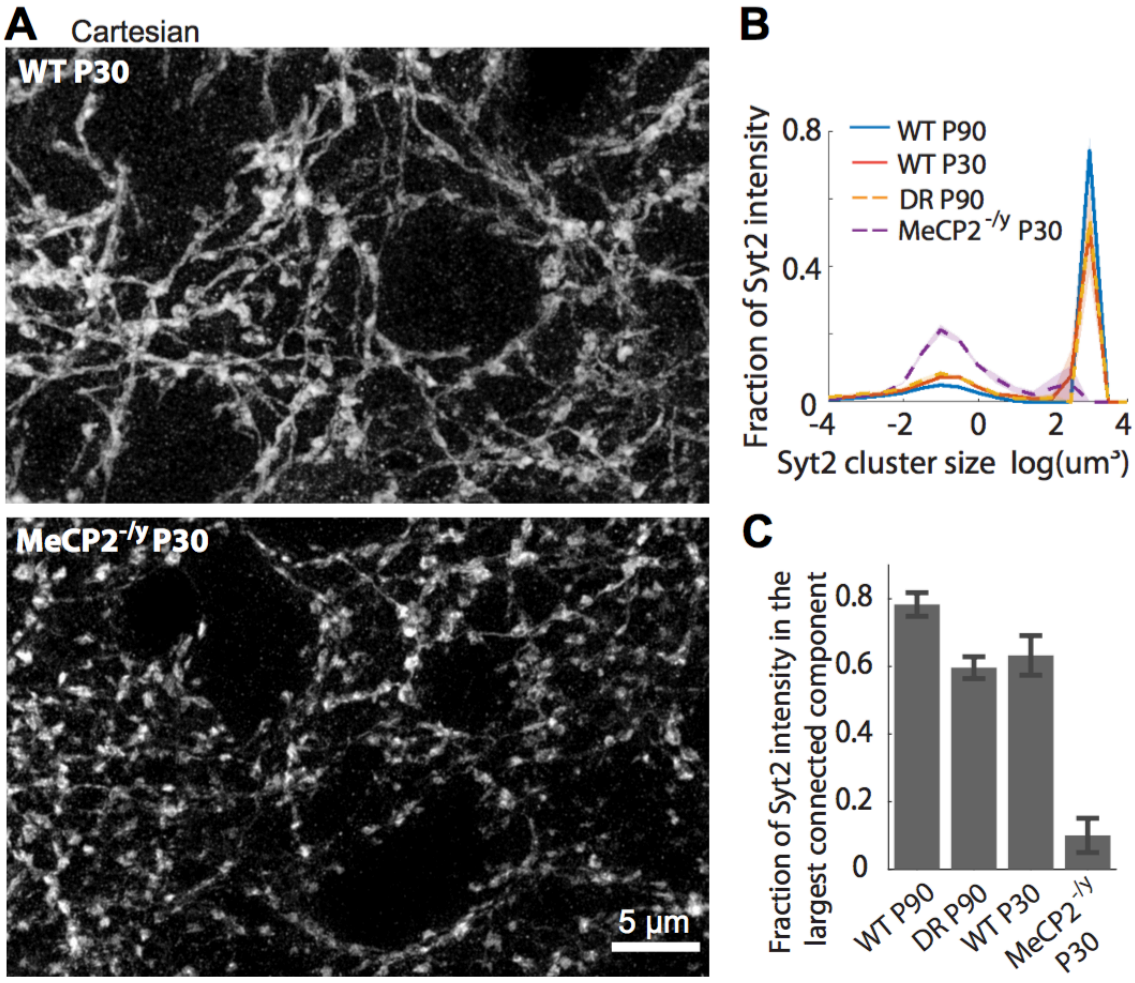

Figure S7. The morphology of the Syt2 signal is strongly altered throughout layer 4 in visual cortex in the MeCP2$^{-/y}$ mice. (A) Maximum intensity projection images of the Syt2 signal in Cartesian coordinates for wild-type (WT) (top) and MeCP2$^{-/y}$ (bottom) P30 samples in representative regions within layer 4 of V1 not necessarily surrounding PV+ cells. **(B)** The distributions of the Syt2 cluster sizes for WT P90 (blue), WT P30 (red), dark-reared (DR) P90 (yellow) and MeCP2$^{-/y}$ P30 (purple) samples for the entire imaged ~100 µm x 100 µm x 20 µm regions. Data are plotted as the mean across imaged regions with the s.e.m. shown as shaded regions. (n = 5 - 6 regions for each condition). **(C)** Fraction of Syt2 signals within each imaged region that is in the largest connected component for WT P90, WT P30, DR P90, and MeCP2$^{-/y}$ P30 samples. Graph shows mean across the imaged regions and the error bars are the s.e.m. (n = 5 - 6 regions for each condition).

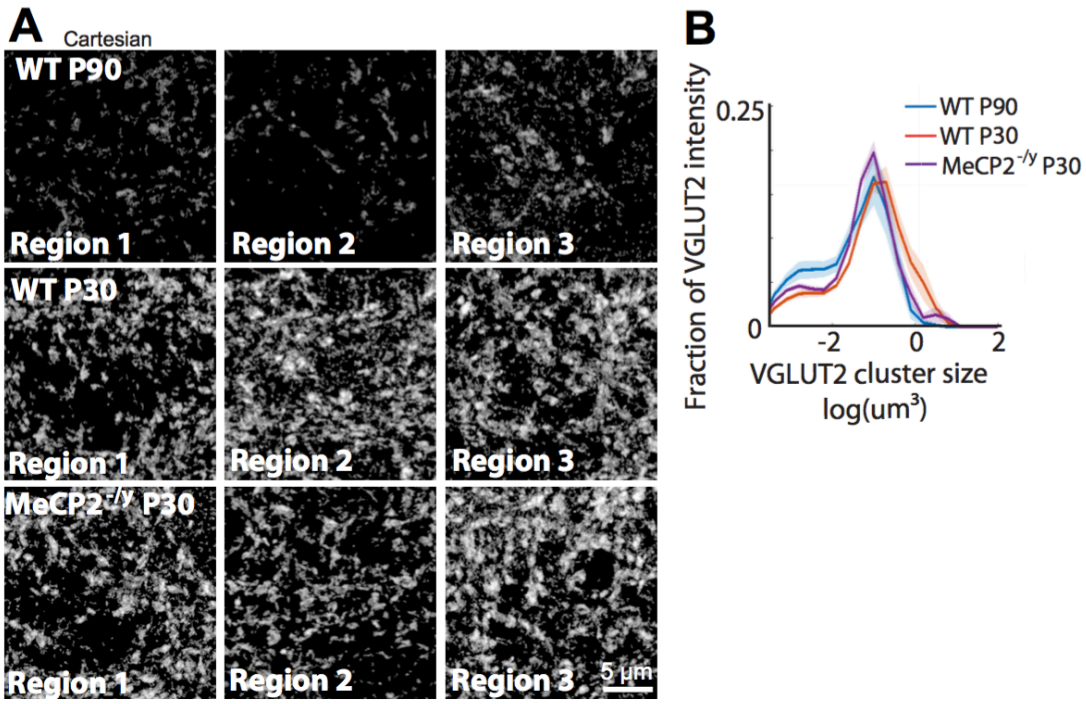

Figure S8. VGLUT2 signal surrounding PV+ cells is increased but shows similar morphology at P30 and in MeCP2$^{-/y}$ P30 animals. (A) Maximum intensity projection STORM images of the VGLUT2 signal in Cartesian coordinates surrounding representative WFA+ PV+ cells in animals across three conditions: wild-type (WT) P90 (top row), WT P30 (second row), and MeCP2$^{-/y}$ P30 (bottom row). To reduce the background in the VGLUT2 maximum intensity projections through thick volumes of tissue (5 µm), small clusters <(70 nm)^3 in volume were removed. **(B)** The distributions of the VGLUT2 cluster sizes for WT P90 (blue), WT P30 (red), and MeCP2$^{-/y}$ P30 (purple) samples for the regions surrounding each WFA+ PV+ cell. Data are plotted as the mean across imaged regions with the s.e.m. shown as shaded regions. (n = 16 – 30 regions for each condition).

References

1. Guy J, Hendrich B, Holmes M, Martin JE, & Bird A (2001) A mouse Mecp2-null mutation causes neurological symptoms that mimic Rett syndrome. *Nat Genet* 27(3):322-326.

2. Sigal YM, Speer CM, Babcock HP, & Zhuang X (2015) Mapping Synaptic Input Fields of Neurons with Super-Resolution Imaging. *Cell* 163(2):493-505.

3. Holden SJ, Uphoff S, & Kapanidis AN (2011) DAOSTORM: an algorithm for high-density super-resolution microscopy. *Nat Methods* 8(4):279-280.

4. Babcock H, Sigal YM, & Zhuang X (2012) A high-density 3D localization algorithm for stochastic optical reconstruction microscopy. *Opt Nanoscopy* 1(6).

5. Saalfeld S, Fetter R, Cardona A, & Tomancak P (2012) Elastic volume reconstruction from series of ultra-thin microscopy sections. *Nat Methods* 9(7):717-720.